






Article

SrMnO₃/Functionalized h-BN Composite Modified Disposable Sensor for the Voltammetric Determination of Furaltadone Antibiotic Drug

Krishnan Venkatesh ¹, Ramachandran Rajakumaran ², Shen-Ming Chen ², Periyakaruppan Karuppasamy ³, Artur Banach ⁴, Wedad A. Al-Onazi ⁵, Selvam Sonadevi ⁶, Nattamai Perumal Krishnan ^{7,*}, Chun-Chen Yang ^{8,9}, Chelladurai Karuppiyah ⁸ and Sayee Kannan Ramaraj ^{1,*}

- ¹ PG and Research Department of Chemistry, Thiagarajar College, Madurai 625009, Tamil Nadu, India
² Department of Chemical Engineering and Biotechnology, National Taipei University of Technology, No. 1, Section 3, Chung-Hsiao East Road, Taipei 10608, Taiwan
³ Department of Chemistry, Dayananda Sagar College of Engineering, Bangalore 760058, Karnataka, India
⁴ Department of Biology and Biotechnology of Microorganisms, Institute of Biological Sciences, Faculty of Medicine, The Jhon Paul II Catholic University of Lublin, Konstantynow 11, 20-708 Lublin, Poland
⁵ Department of Chemistry, College of Science, King Saud University, P.O. Box 22452, Riyadh 11495, Saudi Arabia
⁶ Department of Chemistry, Vyasa Arts and Science College for Women, Vasudevanallur, Tirunelveli 627758, Tamil Nadu, India
⁷ Department of Chemistry, Sourashtra College, Pasumalai, Madurai 625004, Tamil Nadu, India
⁸ Battery Research Center of Green Energy, Ming Chi University of Technology, New Taipei City 24301, Taiwan
⁹ Department of Chemical Engineering, Ming Chi University of Technology, New Taipei City 24301, Taiwan
* Correspondence: krishyaas@gmail.com (N.P.K.); sayeekannanramaraj@gmail.com (S.K.R.)



Citation: Venkatesh, K.; Rajakumaran, R.; Chen, S.-M.; Karuppasamy, P.; Banach, A.; Al-Onazi, W.A.; Sonadevi, S.; Krishnan, N.P.; Yang, C.-C.; Karuppiyah, C.; et al. SrMnO₃/Functionalized h-BN Composite Modified Disposable Sensor for the Voltammetric Determination of Furaltadone Antibiotic Drug. *Catalysts* **2022**, *12*, 1494. <https://doi.org/10.3390/catal12121494>

Academic Editor: Barbara Mecheri

Received: 6 October 2022

Accepted: 18 November 2022

Published: 22 November 2022

Publisher's Note: MDPI stays neutral with regard to jurisdictional claims in published maps and institutional affiliations.



Copyright: © 2022 by the authors. Licensee MDPI, Basel, Switzerland. This article is an open access article distributed under the terms and conditions of the Creative Commons Attribution (CC BY) license (<https://creativecommons.org/licenses/by/4.0/>).

Abstract: Improper disposal of pharmaceutical drugs, including antibiotics, can affect the ecological system and generate serious health problems for living organisms. In this work, we have developed an electrochemical sensor based on a strontium manganese oxide/functionalized hexagonal boron nitride (SrMnO₃/f-BN) electrocatalyst for the detection of the antibiotic drug furaltadone (FLD). Various analytical techniques were used to characterize the physicochemical properties of the as-prepared SrMnO₃/f-BN composite. The as-fabricated SrMnO₃/f-BN composite electrode showed excellent sensing activity towards FLD, with a wide linear range (0.01–152.11 μM) and low detection limit (2.0 nM). The sensor exhibited good selectivity towards FLD for detection in the presence of various interfering species (nitro compounds, metal ions, and biological compounds). Interestingly, real-time analysis using the proposed SrMnO₃/f-BN composite was able to determine the FLD content in human urine and wastewater samples with good recovery. Hence, the as-developed SrMnO₃/f-BN modified sensor could be viable in practical applications to target the antibiotic drug FLD in both human fluids and environmental samples.

Keywords: SrMnO₃ perovskites; electrochemical sensor; voltammetric detection; pharmaceutical drugs

1. Introduction

Furaltadone (FLD) is a synthetic antibiotic drug used in the veterinary field to treat bacterial diseases such as fowl cholera, coccidiosis, and blackhead disease [1,2]. High-level doses of FLD in animals lead to severe side effects, including mutagenesis, hemolytic anemia, thrombopenia, insanity, and chronic toxicity, and causes cancer in rats and mice [3,4]. Due to the adverse effects of this drug, most countries have banned it; however, FLD is used in several food products at the quantitative level [5,6]. Thus, the determination of FLD in food samples is an essential need; detection follows Rapid Alert System for Food and Feed (RASFF) standards for its residues in poultry, aquatic, and all animal products due

to its low cost and pharmaceutical properties [7,8]. Several methods have been utilized to detect FLD in food samples, including high-performance liquid chromatography (HPLC), mass spectroscopy, spectrophotometry, immunoassay, electrochemical methods, and others. Among them, electrochemical techniques are inexpensive, easy to perform, selective, and sensitive, providing fast detection and reliability compared with other techniques. However, in this electrochemical method, modified electrodes play a vital role in improving detection sensitivity compared to conventional unmodified electrodes [5,9,10].

In recent decades, perovskite (ABO_3)-type materials have drawn considerable attention to various applications, including solar cells, batteries, gas sensors, water splitting, photocatalysis, and biosensors [11–16]. This is due to their attractive properties, such as high surface area, excellent catalytic property, and high stability [17,18]. The ABO_3 type of perovskite material is entirely different from ordinary metal oxides. In the ABO_3 structure, A is built with a larger cation size, whereas B is a smaller cation; both the cations are interlinked with the oxygen anions. Generally, the smaller cation in ABO_3 improves the redox properties of the material, and the larger size cation is usually attached to the edge [19–23]. According to the literature review, the larger cations of alkaline earth metals ($A = Sr, Ba, Ca, \text{etc.}$) containing $AMnO_3$ perovskite structures have attracted attention due to their excellent electrocatalytic activity, thermal stability, lower bandgap (E_g), and large surface area [24–28]. Numerous synthesis methods, including reverse microemulsion, greener synthesis, electrospinning, and the Pechini, wet chemical, and hydrothermal techniques have been developed to prepare $AMnO_3$ nanomaterials for various applications such as photocatalysis, lithium-ion batteries, water splitting, and sensors [28–34]. This study demonstrates a simple co-precipitation method to prepare strontium manganese oxide ($SrMnO_3$) perovskite materials. Among the synthesis processes mentioned above, co-precipitation is a cost-effective and straightforward method that can provide a good and high yield of $SrMnO_3$ particles. $SrMnO_3$ has different polymorphs, such as cubic, 4H, and 6H hexagonal structures. Among them, the 4H hexagonal structure is thermodynamically stable. It has been widely used in various applications, including absorbents, catalysis, sensors, photocatalysis, supercapacitors, dye-sensitized solar cells, and energy storage devices [12,35–42]. However, all these types of perovskite materials with a high melting point should be calcined at high temperatures for a long time, leading to a low surface area [17,43]. Supporting matrixes, such as graphene, reduced graphene oxide, carbon nanofiber, boron nitride, etc., can be incorporated with these perovskite materials to improve their properties [44–48]. These matrix-based hybrid catalysts show enhanced electrochemical properties thanks to their synergistic effects.

Hexagonal boron nitride (h-BN) is a similar structural analog of graphite in which B atoms are present above/below the N-atoms in the adjacent layers of h-BN. In addition, h-BN is a highly stable structure compared to cubic-boron nitride and wurtzite-boron nitride in standard conditions. It has a wide optical E_g range from 2.45 to 5.4 eV. Due to this wide band-gap energy, h-BN exhibits essential characteristics such as high mechanical strength, thermal conductivity, and good electrical, optical, and chemical properties. Therefore, it is widely used in nanotechnology. Furthermore, h-BN presents an easily moveable free electron, enhancing charge transfer mobility and improving the intrinsic electrocatalytic activity performance. Furthermore, exfoliated h-BN offers a high surface area that can facilitate better electrochemical performance [49–55].

In this work, we synthesized an $SrMnO_3$ perovskite and functionalized h-BN (f-BN) composite material by following the co-precipitation and ultrasonication methods. The as-prepared $SrMnO_3/f$ -BN composite was successfully fabricated and used as a modified electrode for sensing the drug FLD. The available literature on the state-of-the-art in this domain shows very few reports on FLD detection; these use various nanomaterials coupled to electrochemical methods. For example, nanomaterials based on $ZnO-ZnCo_2O_4$, $Fe_{0.11}V_2O_{5.16}$ wrapped porous graphene oxide nanosheets, $Ni/TiO_2/MWCNTs$, and Co_2SnO_4/SnO_2 have been used for FLD detection; however, all of these exhibit poor sensitivity and low detection parameters [56–59]. Therefore, finding a superior novel hybrid electrocatalyst to

enhance the sensitivity of FLD sensing is challenging work. Surprisingly, our fabricated SrMnO₃/*f*-BN composite-based FLD sensor is able to deliver excellent sensing parameters such as a very low detection limit with a wide linear range, high sensitivity, better selectivity, and excellent recoveries in practical analysis.

2. Results and Discussion

2.1. Materials Characterization

The functional group analysis of the as-prepared SrMnO₃, *f*-BN, and SrMnO₃/*f*-BN composite was confirmed by FT-IR spectroscopy, as shown in Figure 1A. The FTIR spectrum of SrMnO₃ (Figure 1A(a)) exhibited a stretching frequency band at 660 cm⁻¹, ascribed to the Mn-O bond formation. The bending vibration mode of the O-B-O bond appeared at 545 cm⁻¹, which resembles the BO₆ octahedron in the SrMnO₃ perovskite structure. The bands at 580 and 450 cm⁻¹ originate from the vibration of metal-oxygen bonds with a spinel cubic structure of tetrahedral and octahedral sites. The broad bands at 3100 and 3400 cm⁻¹ are attributed to the hydroxyl groups. In the FT-IR spectrum of *f*-BN (Figure 1A(b)), the observed bands at 520, 620, 820, 1580, and 3180 cm⁻¹ correspond to B-N, B-O, B-N-B, B-NH₂, and B-OH bond formation, respectively. The FT-IR spectrum of the SrMnO₃/*f*-BN composite showed similar characteristic vibrational peaks, with high intensity and slight shift as compared to the FT-IR spectrum of SrMnO₃ and *f*-BN, as shown in Figure 1A(c). The FT-IR spectrum of the SrMnO₃/*f*-BN composite revealed the shift in peak values due to the strong interaction between SrMnO₃ and *f*-BN.

The XRD pattern of SrMnO₃, *f*-BN, and SrMnO₃/*f*-BN composite is depicted in Figure 1B. The XRD pattern of SrMnO₃ (Figure 1B(a)) exhibits prominent diffraction peaks at the 2θ angles of 19.05°, 27.44°, 32.92°, 35.32°, 39.71°, 43.34°, 44.46°, 48.96°, 49.09°, 54.47°, 55.35°, 56.11°, 58.86°, 60.37°, 61.26°, 62.50°, 64.87°, 66.74°, and 69.11°, corresponding to the (002), (102), (110), (103), (004), (202), (104), (203), (210), (105), (212), (204), (300), (213), (006), (302), (205), (214), and (220) planes, respectively. All these diffraction planes are well matched with the standard pattern of JCPDS card No. 84-1612, ascribed to the hexagonal perovskite structure with a space group of P6₃/mmc. The (110) plane shows the maximum intensity, with the d-spacing of 2.46 Å, and the corresponding lattice parameters are obtained at about a = b = 5.44 Å and c = 9.07 Å. Furthermore, the crystallite size of the as-prepared SrMnO₃ perovskite particle was calculated to be 13 nm based on the (110) plane using the Scherrer method. In addition, Figure 1B(b) shows the XRD pattern of *f*-BN, which exhibits the diffraction of 2θ angles at 26.96°, 41.96°, 50.23°, and 55.33°, corresponding to the hexagonal structure of boron nitride with the crystal planes of (002), (100), (102), and (004), respectively. The corresponding pattern is well-matched with the standard file of JCPDS card No. 73-2095 and the space group of P-6m2. In addition, the XRD pattern of the SrMnO₃/*f*-BN composite shows a slight decrease in crystallinity planes, with a lower angle shift in Figure 1B(c). However, the peaks at (002) and (100) planes continue to exist in the pattern, indicating the incorporation of the *f*-BN nanosheet with the SrMnO₃ microsphere.

Figure 1C shows the Raman spectra of SrMnO₃, *f*-BN, and SrMnO₃/*f*-BN composite. The hexagonal phase of the SrMnO₃ (Figure 1C(a)) exhibits eight Raman active modes, namely, modes 2A_{1g} + 2E_{1g} + 4E_{2g} [12,41,42]. The peak at 339 cm⁻¹ is assigned to the E_{1g} mode, suggesting Mn ion displacements. At the same time, the peaks at higher frequencies indicate that the oxygen ion is involved in the MnO₆ octahedral. This suggests that the oxygen ions can be distinguished as O (1) and O (2) ions, with both involved in face sharing and corner-sharing of the adjacent octahedral. The O (1) oxygen ions alone provide Raman active modes. Significantly, the peak around 435 cm⁻¹ is assigned to the octahedral tilting E_{1g} and bending E_{2g} modes. The high-intensity peaks at 593 and 642 cm⁻¹ are ascribed to the asymmetric E_{2g} and symmetric A_{1g} octahedral stretching modes associated with the Sr and Mn ions, respectively. The Raman spectrum of *f*-BN (Figure 1C(b)) exhibits a sharp peak at 1369 cm⁻¹, assigned to the E_{2g} mode and comparable to the G-band of graphene. The Raman spectrum of the SrMnO₃/*f*-BN composite (Figure 1C(c)) shows the

typical characteristic bands of SrMnO₃ and *f*-BN mentioned above, which display a decrease in intensity due to the strong interaction of the *f*-BN nanosheet with the SrMnO₃ microspheres.

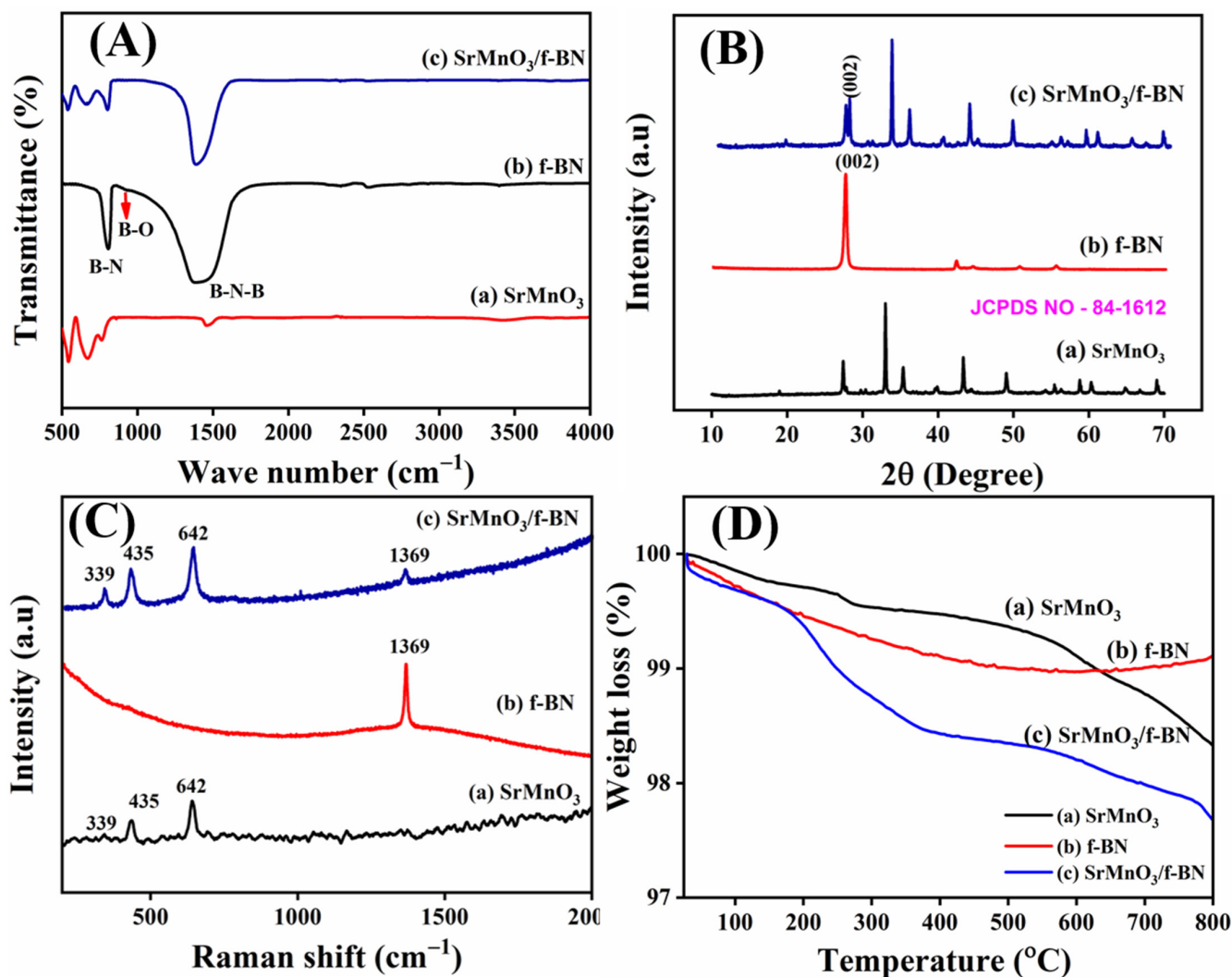


Figure 1. (A) FT-IR spectrum, (B) XRD pattern, (C) Raman spectrum, and (D) TGA curves of (a) SrMnO₃, (b) *f*-BN, and (c) SrMnO₃/*f*-BN composite.

The thermal stability of SrMnO₃, *f*-BN, and SrMnO₃/*f*-BN was characterized by the thermogravimetric analysis (TGA) method. Figure 1D(a) displays the three different weight-loss stages: (i) the first weight loss of 11.4% in the temperature range up to 150 °C corresponds to the loss of surface adsorbed water molecules' evaporation; (ii) the second weight loss between 250 to 400 °C involves the carbonyl of SrMn(CO₃)₂ followed by decomposition of organic contents; and (iii) the final weight loss at 400–700 °C is attributed to the strontium precursor and manganese decomposition. In addition, Figure 1D(b) shows *f*-BN nanosheet thermal degradation at 200 °C, which can be attributed to disclosing of the peroxide moiety and decomposition of the oxygen group. Interestingly, the thermal decomposition behavior of the SrMnO₃/*f*-BN composite (Figure 1D(c)) exhibits similar weight loss as the pristine SrMnO₃ and *f*-BN, confirming the incorporation of *f*-BN into the SrMnO₃ microsphere particles.

Furthermore, BET measurements were performed for SrMnO₃, *f*-BN, and SrMnO₃/*f*-BN composite materials based on the N₂ adsorption/desorption isotherm method. The results can be seen in Figure S1. From the BET analysis, the specific surface area of the SrMnO₃ and SrMnO₃/*f*-BN is 8.76 and 10.25 m²/g, respectively, while the pore size and pore volume of

the SrMnO₃/f-BN composite is calculated as 13.23 nm and 1.37 cm³/g, respectively. The larger surface area and porous are attributed to the formation of different active sites for enhancing the electrocatalytic activity of the material due to the mobility of ions/electrons.

FE-SEM was used to analyze the surface morphology of SrMnO₃, f-BN, and SrMnO₃/f-BN composite samples. Figure 2A–C shows a homogeneous microsphere morphology formed through the integration of SrMnO₃ primary nanoparticles (particle size range of 100–250 nm). However, the average size of microsphere particles is calculated at approximately 6 μm. Figure 2D–F shows the FE-SEM images of the f-BN, which exhibit the stacked flakes of exfoliated BN due to the combination of oxygen functionalities. The elemental mapping proves the oxygen functionalities, and their atomic percentages are provided in Figure S3. Figure 2G,H displays FE-SEM images of the SrMnO₃/f-BN composite, confirming the decoration of SrMnO₃ microsphere particles on f-BN flakes. This could be valuable in the creation of a substantial surface area in the composite for improving its electrochemical performance. Furthermore, the elemental mapping and EDX spectrum confirmed the distribution of elements such as Sr (Strontium), Mn (Manganese), O (Oxygen), B (boron), and N (Nitrogen) in the SrMnO₃/f-BN composite. The corresponding results are shown in Figure S2.

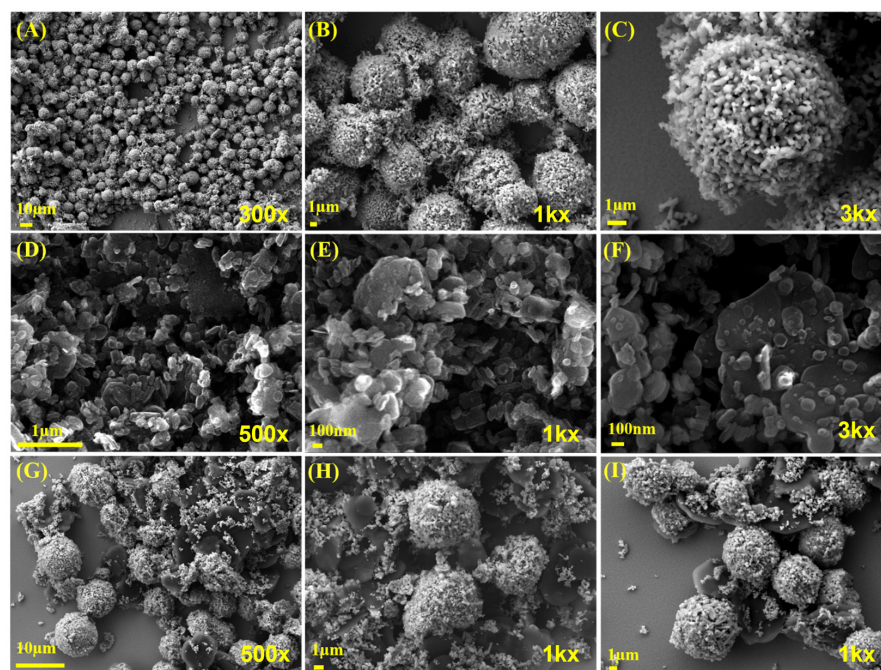


Figure 2. (A–C) High (1k× and 3k×) and low (300× and 500×) magnification of FE-SEM image of SrMnO₃; examples of (D–F) f-BN and (G–I) SrMnO₃/f-BN composite.

2.2. Electrochemical Properties

The charge transfer resistance property of the SrMnO₃/f-BN nanocomposite electrode was investigated by electrochemical impedance spectroscopy, for which it was examined in 5 mM [Fe(CN)₆]^{3−/4−} with 0.1 M KCl solution. For comparison, the Nyquist plots of the different modified SPCEs (screen-printed carbon electrodes), such as bare SPCE, SrMnO₃/SPCE, f-BN/SPCE, and SrMnO₃/f-BN/SPCE, were evaluated (Figure 3). The plots show a semicircle in the high-frequency regions and inclined lines in the low-frequency regions. These spectra illustrate that the charge transfer resistance (R_{ct}) value of SrMnO₃/f-BN/SPCE is 803.41 Ω, which is lower than bare SPCE (3876.53 Ω), SrMnO₃/SPCE (2794.61 Ω), and f-BN/SPCE (1794.52 Ω), representing the superior electron conductivity of the SrMnO₃/f-BN nanocomposite modified SPCE.

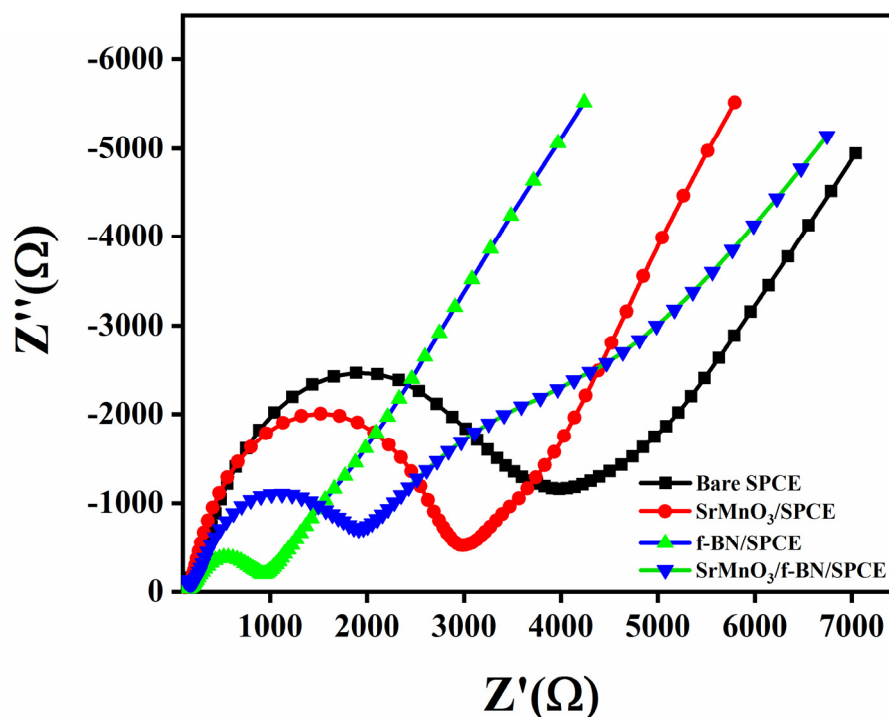
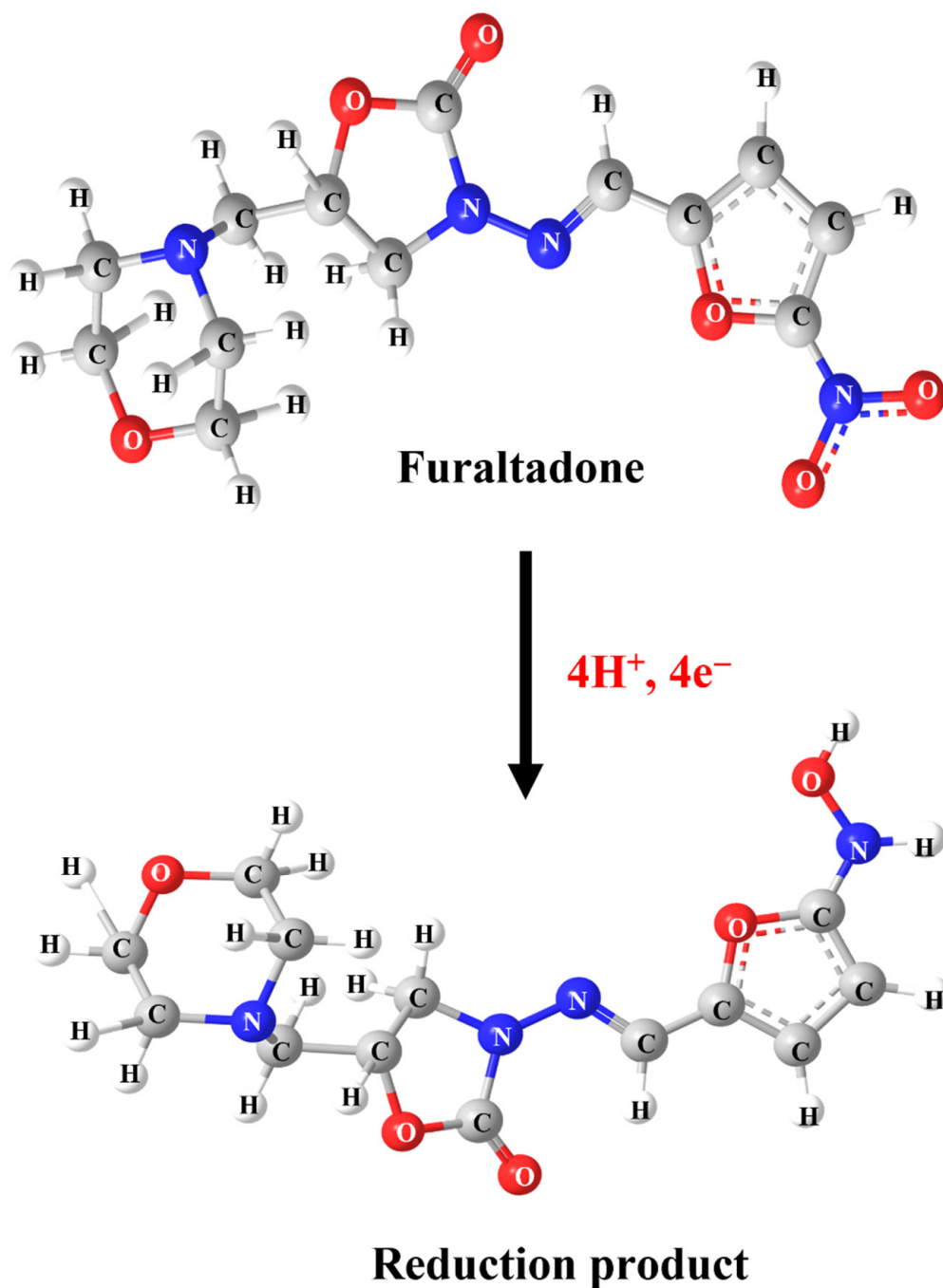


Figure 3. Nyquist plots of bare SPCE, SrMnO₃/SPCE, f-BN/SPCE, and SrMnO₃/f-BN/SPCE in 5 mM [Fe(CN)₆]^{3−/4−} with 0.1 M KCl solution.

2.2.1. Electrochemical Behavior of FLD

Cyclic voltammetry (CV) is an essential technique in electrochemical methods, as it is easier to understand the initial electrochemical behavior, and the resulting information is rather useful for performing electrochemical studies about complicated electrode reactions. Therefore, preliminary electrochemical experiments were carried out using the CV technique to examine the electrochemical behavior of FLD. Beforehand, different operational electrodes were fabricated, such as bare SPCE, pristine boron nitride modified SPCE (BN/SPCE), *f*-BN/SPCE, and SrMnO₃/*f*-BN/SPCE. The CV curves were recorded at a fixed scan rate of 50 mV/s in pH 7 containing 200.0 μM FLD sensing sample. The obtained CV signals are shown in Figure 4A. The CV results show that the bare SPCE has a weak reduction peak at −0.475 V with a current intensity of −8.01 μA, which is due to poor electron transfer mobility between the unmodified SPCE surface and FLD. On the other hand, the BN/SPCE shows a slightly better cathodic current response than the bare SPCE, at −0.473 V, with a current density of about −8.66 μA. This might be due to the electrical insulating property of BN, which bears a wide bandgap; this may resist the transfer of electrons towards the reduction of FLD. Despite this, the BN consists of covalently bounded B (boron) and N (nitrogen) atoms, which disturb the electronic states of symmetry as well as their electronic arrangement, suggesting the narrowing of the sp²-derived π bands. The SrMnO₃/SPCE shows a well-resolved cathodic current amplitude of −14.85 μA at −0.5311 V, corresponding to the superior electrical conductivity of the SrMnO₃ nanospheres, and it retains the covalent bonding of Mn-O bonds and Sr²⁺ ions in the crystal lattice, providing faster electron transferability for FLD sensing. Along with this, the SrMnO₃ nanospheres access to the transition of manganese ionic oxidation states between Mn³⁺ ⇌ Mn⁴⁺ is able to accelerate the electrocatalysis property, promoting the reduction of FLD. *f*-BN/SPCE exhibits better electrocatalytic activity than BN/SPCE thanks to the effective functionalization of the BN surface with OH functional groups, tremendously increasing the boron radicals at the edges to create defective sites. This electrochemically enables advantageous FLD sensing, with a current response of about −15.71 μA at −0.46 V. Finally, the SrMnO₃/*f*-BN/SPCE shows higher cathodic current

waves of about $-23.01 \mu\text{A}$ at a cathodic potential of -0.465 V . This cathodic CV signal is attributed to the direct electrocatalytic reduction of the nitro group (NO_2) of FLD into the hydroxylamine group, with the elimination of the water molecule accompanied by the participation of an equal number of electron (4H^+) and proton (4e^-) transfer processes (Scheme 1).



Scheme 1. Electrochemical reduction mechanism of FLD.

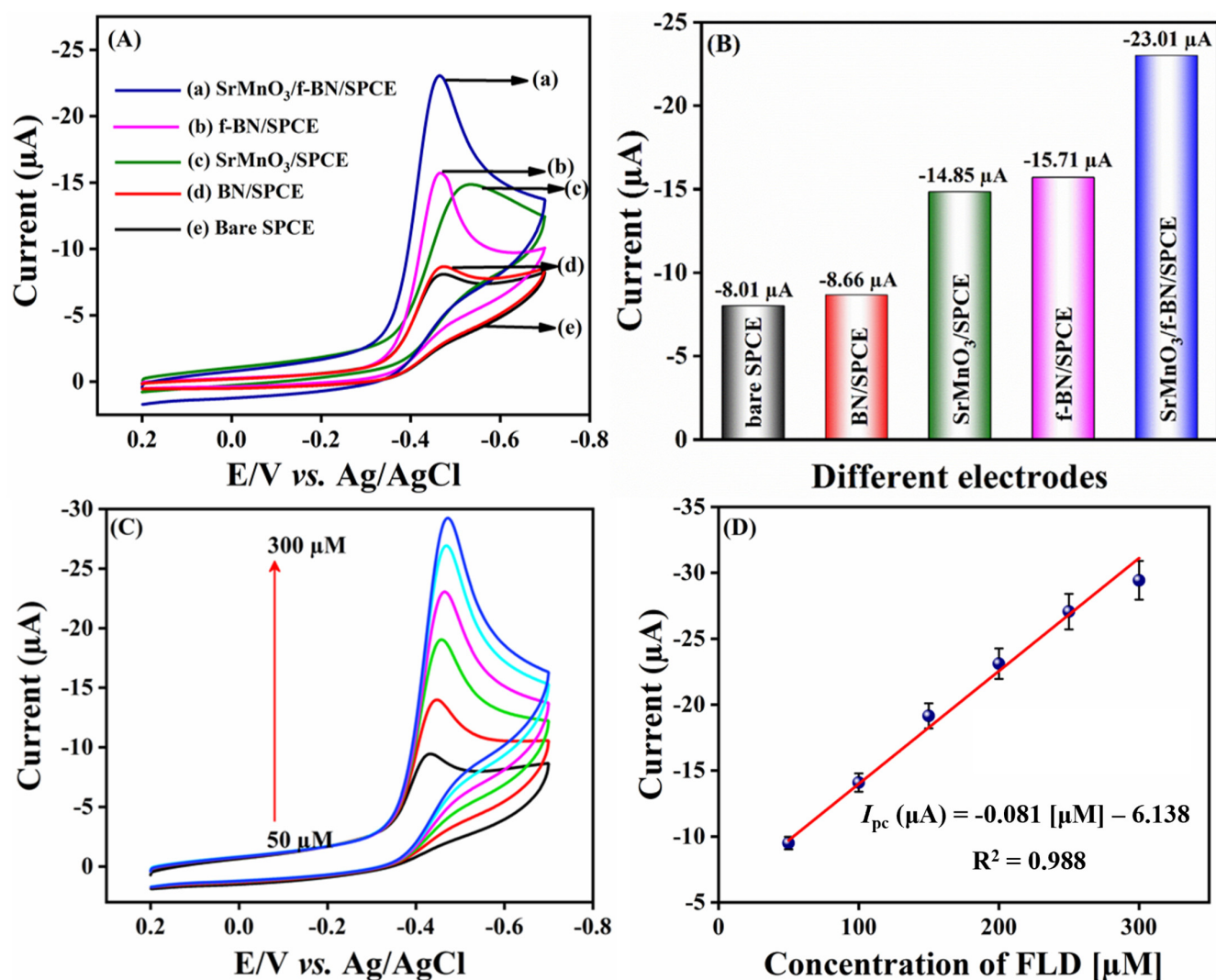


Figure 4. (A) CVs of different modified SPCE of FLD detection in 0.1 M PBS (pH 7) with 200.0 μM of FLD; scan rate 50 mV/s. (B) Bar diagram of different electrodes vs. current (μA). (C) CVs for the addition of different concentrations of FLD (50.0–300.0 μM); scan rate 50 mV/s. (D) Linear calibration plot of concentration of FLD (μM) vs. current (μA) for three replicative measurements ($n = 3$).

At the same time, no oxidation peak current response was observed while performing the anodic scan, suggesting an irreversible electron transfer chemical reaction process. From the above-obtained results and findings, it is clear that the SrMnO₃/f-BN/SPCE delivered a beneficial reduction in peak current response, and the lowest cathodic potential for FLD detection over that of other electrodes (bare SPCE, BN/SPCE, f-BN/SPCE) can be retained. Additionally, the electrochemical reduction of FLD occurs at the surface of SrMnO₃/f-BN/SPCE due to the excellent electrostatic interaction between the FLD and the electrode surface, confirming the improved electrocatalytic property of the SrMnO₃/f-BN composite. This synergistic activity is due to the interaction of the d_z^2 of the transition metal orbitals and the B- p_z , N- p_z orbitals of f-BN. These bonds are responsible for the prominent modification of the electronic properties of f-BN aided on the 3d, 4d, and 5d transition metal surfaces, which enhances the combinational electrocatalytic activity of the composite and in turn facilitates the effective sensing of FLD. The obtained current response for different electrodes is represented as a bar diagram in Figure 4B.

2.2.2. Effect of Concentration

The influence of concentration on SrMnO₃/f-BN/SPCE was examined using CV by adding FLD concentration from 50.0 to 300.0 μM. Figure 4C depicts the CV curves of various concentrations of FLD; it can be seen that the cathodic peak current of FLD increases linearly with increasing concentration of FLD. This is due in part to the good electrode–electrolyte interface, as the optimal diffusion length favors sensing of the FLD in the electrochemical system. In addition, an excellent linear relationship can be observed in Figure 4D, demonstrating that the reduction of current signal waves is directly proportional to the concentration of FLD. There is a linear regression equation of $I_{pc} = -0.081 \text{ FLD } [\mu\text{M}] - 6.138$ with correlation coefficient of $R^2 = 0.988$. From the concentration CV studies, the as-prepared composite acts as a potential electrode material as well as an excellent electron mediator, as it possesses chemically electroactive sites via the functionalization of BN with active functional groups. In addition, the electrical conductivity is further enhanced by the SrMnO₃ nanospheres, which allow faster electron transfer processes for FLD detection.

2.2.3. Effect of pH and Scan Rates

In electrochemical detection systems, pH is one of the most important parameters for developing an electrochemical sensor, as it affects the sensitivity and electrochemical behavior of FLD at the surface of SrMnO₃/f-BN/SPCE. Figure 5A displays the CV response of 200.0 μM FLD for different pH values (pH 3.0, pH 5.0, pH 7.0, pH 9.0, and pH 11.0) recorded at a scan rate of 50 mV/s. It can be seen that the cathodic current response of FLD gradually increases from pH 3.0 to 7.0, and gains a maximum current intensity at pH 7.0; subsequently, the current amplitude decreases, moving towards a higher pH value in Figure 5B. Following this pH test, pH 7.0 was chosen as a supporting electrolyte for electrochemical experiments. The slope of the linear plot between cathodic peak potential (E_p) and pH (Figure S4) demonstrates that the electrochemical performance of FLD is strongly pH-dependent [46] and the hydrogen ion (H^+) concentration influences the reaction rate of the constructed electrode. The electrode kinetics property of FLD at the SrMnO₃/f-BN/SPCE was studied by recording the CV signals in pH 7.0 at different scan rates from 20 to 200 mV/s in the electrochemical cell containing 200.0 μM FLD. Figure 5C shows the CV signal wave concerning the applied potential, which is equivalent to the cathodic reduction reaction of FLD. It can be observed that the cathodic current density ramps up accordingly upon increasing the scan rate from 20 to 200 mV/s. In addition, the cathodic peak potential shift towards the negative side of the potential window affirms the irreversible electrode process. Figure 5D represents a good linear relationship between the FLD peak current intensity and the scan rate (ν), with the correlation coefficient $R^2 = 0.997$ and the corresponding linear regression equation expressed as $I_{pc} = -0.078 \nu - 10.77$. These results show that the reduction process of FLD catalyzed by SrMnO₃/f-BN/SPCE is controlled by the adsorption process. The process was further evaluated by plotting the linear relation between the log scan rate ($\log \nu$ (mV/s)) and log current ($\log I$ (μA)), as shown in Figure S5A. The slope of the linear plot clearly confirms that the electrode processes are neither adsorption-controlled (slope = 1) nor diffusion-controlled (slope = 0.5). The slope value (0.35) of Figure S5A shows that FLD detection on SrMnO₃/f-BN modified SPCE favors a diffusion-controlled reaction process. Another linear relation (Figure S5B) is plotted against E_p vs. $\ln \nu$ based on the Laviron Equations (1) and (2):

$$E_{pc} = E^0 + \left(\frac{RT}{\alpha nF} \right) \ln \left(\frac{RTk^0}{\alpha nF} \right) + \left(\frac{RT}{\alpha nF} \right) \ln \nu \quad (1)$$

$$E_{pc} = \frac{2.303RT}{\alpha nF} \quad (2)$$

where R is the gas constant ($8.314 \text{ J mol}^{-1} \text{ K}^{-1}$), T is the temperature (298 K), n is the number of transferred electrons, α is the electron transfer coefficient (0.5), and F is the

Faraday constant is $96,485 \text{ C mol}^{-1}$. The slope of the rate of the linear plot is shown in Figure S5B.

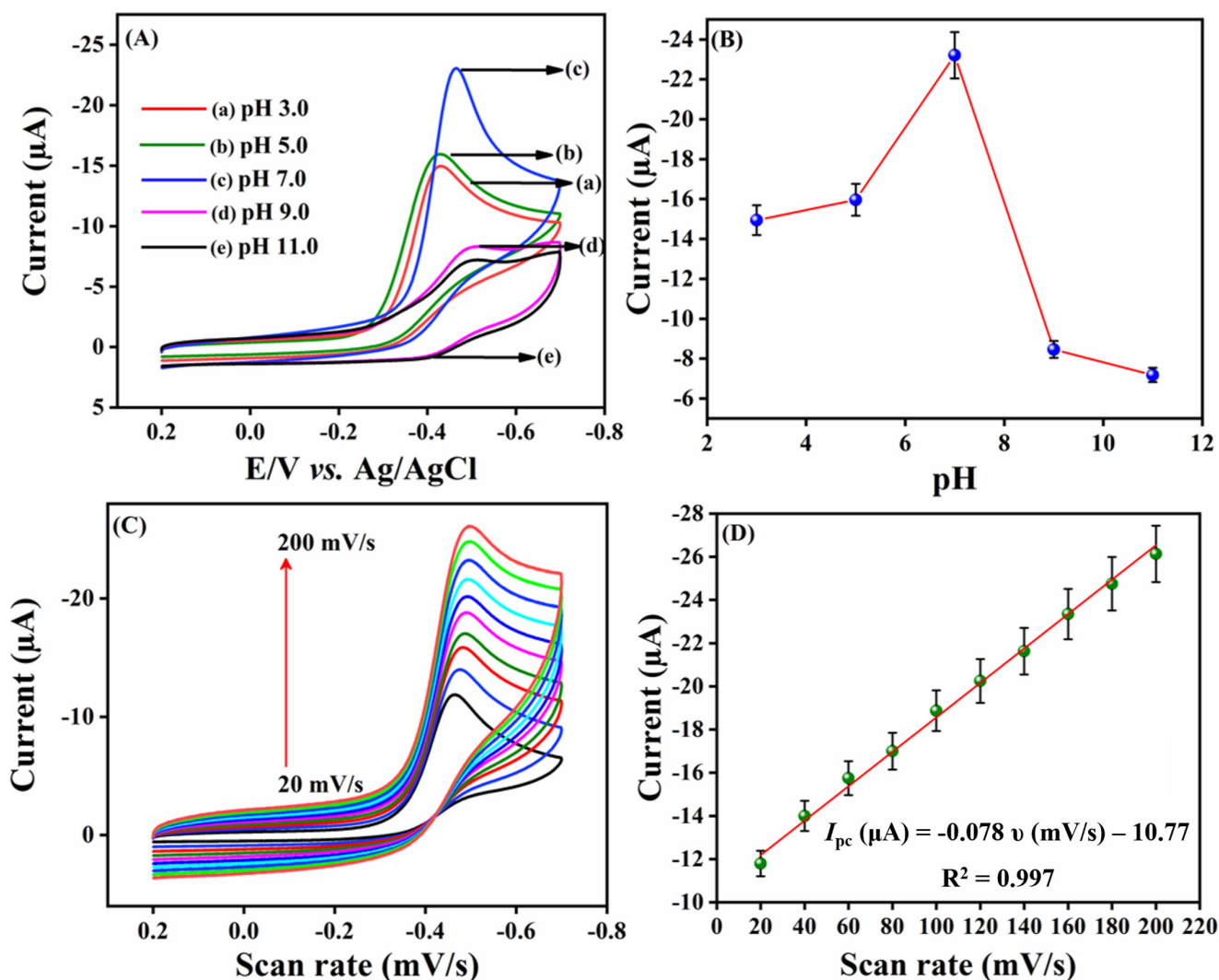


Figure 5. (A) CV current response of different pH (pH 3.0 to pH 11.0) in the presence of 200.0 μM FLD at 50 mV/s. (B) Linear plot of different pH vs. Current (μA). (C) CV profiles of different scan rate in the presence of 200.0 μM FLD in 0.1 M PBS (pH 7.0). (D) Calibration plot of different scan rate (mV/s) vs. current (μA). Three replicative measurements ($n = 3$) were taken.

2.2.4. Differential Pulse Voltammetry (DPV) Analysis

To evaluate the limits of detection and sensitivity, the electroanalytical behavior of $\text{SrMnO}_3/f\text{-BN}$ composite fabricated SPCE was investigated using the DPV technique; the obtained DPV signals are shown in Figure 6A. Initially, the electrolyte solution (pH 7.0) was deoxygenated with massive purity of N_2 gas. Following this process, the voltammogram experiment was recorded by the consecutive addition of analyte concentration from 0.01 to 332.11 μM . Figure 6A represents the DPV amplification waves concerning the successive injection of the target FLD analyte. It can be seen that the cathodic current intensity accelerates linearly with each addition of FLD, governed by the linear regression equation $I_{pc} = -0.1715 \text{ FLD } [\mu\text{M}] - 4.269$ with the correlation coefficient $R^2 = 0.991$ (Figure 6B). The developed sensor exhibits a wide dynamic linear range of detection, from 0.01 to 152.11 μM . The limit of detection of the sensor is calculated using the following equation:

$$\text{LOD} = 3\sigma/\text{slope} \quad (3)$$

where σ is the standard deviation of the background of the three DPV signals and the slope value obtained from the linear plot of peak current (μA) vs. the concentration of FLD (μM). The calculated LOD of the FLD sensor is about 2.0 nM, and its sensitivity (sensitivity = slope/electrode area) is $2.45 \mu\text{A} \mu\text{M}^{-1} \text{cm}^{-2}$. In addition, the modified electrode reduces the mass transfer resistance property due to the synergistic electrocatalytic effect between the *f*-BN and SrMnO_3 nanospheres. From the DPV studies, the fabricated $\text{SrMnO}_3/f\text{-BN}/\text{SPCE}$ sensor reveals its dramatic sensing application towards FLD, with a good catalytic effect affirmed by the rapid electron transfer facilitation of the composite. The electrochemical performance of $\text{SrMnO}_3/f\text{-BN}/\text{SPCE}$ in the detection of FLD was compared with the previously reported FLD sensors, and the results are outlined in Table 1 [9,10,56–59].

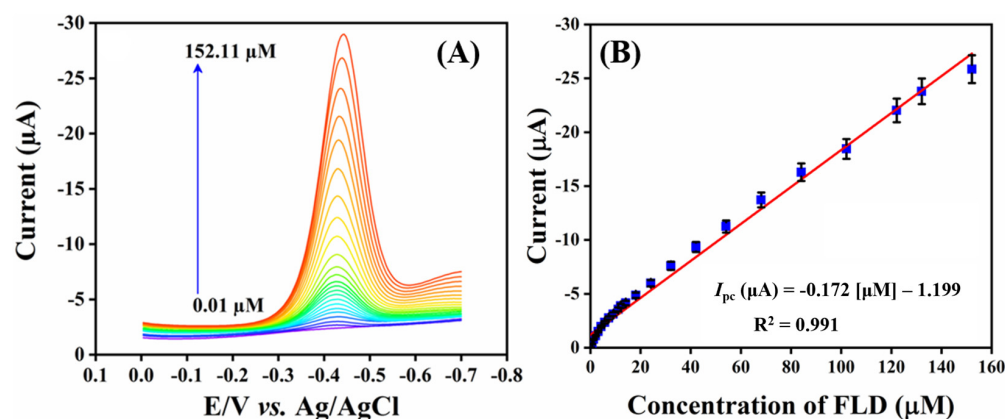


Figure 6. (A) DPV cathodic current response of sequential addition of FLD (0.01–152.11 μM) in PBS (pH 7.0) and (B) the corresponding linear calibration plot of concentration of FLD (μM) vs. current (μA) for three replicative measurements ($n = 3$).

Table 1. Comparison of FLD sensors with different previously-reported modified electrodes.

Working Electrode	Techniques	Linear Range (μM)	LOD (μM)	References
NC-Poly(melamine)/SPCE	ADSV		0.012	[9]
ZnO-ZnCo ₂ O ₄ /GCE	DPV	0.01–4.68; 15.0–100.0	0.034	[56]
Cu/Ni/TiO ₂ /MWCNTs/SPCE	A	10.0–150.0	0.095	[57]
Co ₂ SnO ₄ /SnO ₂ /SPCE	DPV	0.1–73.0; 91.0–1022.0	0.039	[58]
Fe _{0.11} V ₂ O _{5.16} /p-rGO/GCE	A	0.5–84.0; 94.0–1319.0	0.138	[59]
SrMnO ₃ / <i>f</i> -BN/SPCE	DPV	0.01–152.11	0.002	This work

Note: ADSV—Anodic differential stripping voltammetry; DPV—Differential pulse voltammetry; A—Amperometry; LOD—Limit of detection.

2.2.5. Selectivity, Repeatability, and Storage Stability Studies

Selectivity is one of the key factors for the developed sensor, and seems to be the basic requirement for practical applications. Here, the selectivity test was performed using DPV in the existence of interfering compounds, namely, metal ions (Fe^{2+} , Mg^{2+} , Na^+ , NO_2^- , Zn^{2+} , Co^{2+}), biomolecules such as ascorbic acid (AA), uric acid (UA), sucrose (SUC), dopamine (DOP), glucose (GLU), hydrogen peroxide (H_2O_2), lactose (LAC), and citric acid (CA), and nitro compounds such as flutamide (FLU), chloramphenicol (CAP), nitrofurantoin (NFD), 4-nitroaniline (4-NA), and furazolidone (FZ). The DPV signals of $\text{SrMnO}_3/f\text{-BN}/\text{SPCE}$ towards 10.0 μM FLD in the presence of interfering compounds are displayed in Figure 7A–C. It can be seen that the interfering compounds show negligible changes with the main peak current DPV signal of FLD, with an RSD of about 5.95%. Therefore, the developed sensor possesses anti-interference capability towards the selective sensing of FLD. The repeatability experiment was carried out by adding 10.0 μM of FLD in the electrolyte cell, then the DPV signal was recorded continuously over five repeated runs, with each consecutive measurement obtained as DPV signal waves. The results are displayed in

Figure 7D, showing that the fashioned electrode exhibits excellent repeatability with an RSD of about 0.39%. Furthermore, the storage stability of the electrode was tested by adding 10 μM , then obtaining the DPV signal. Afterwards, the DPV signal was measured again over the duration of 10 to 30 days. Interestingly, the cathodic current signal shows only a slight drop in the current response from the initial FLD peak current signal (Figure 7E), with an RSD of about 2.25%. From the above DPV results, the fabricated electrode retains good selectivity, repeatability, and admirable storage stability towards the sensing of FLD.

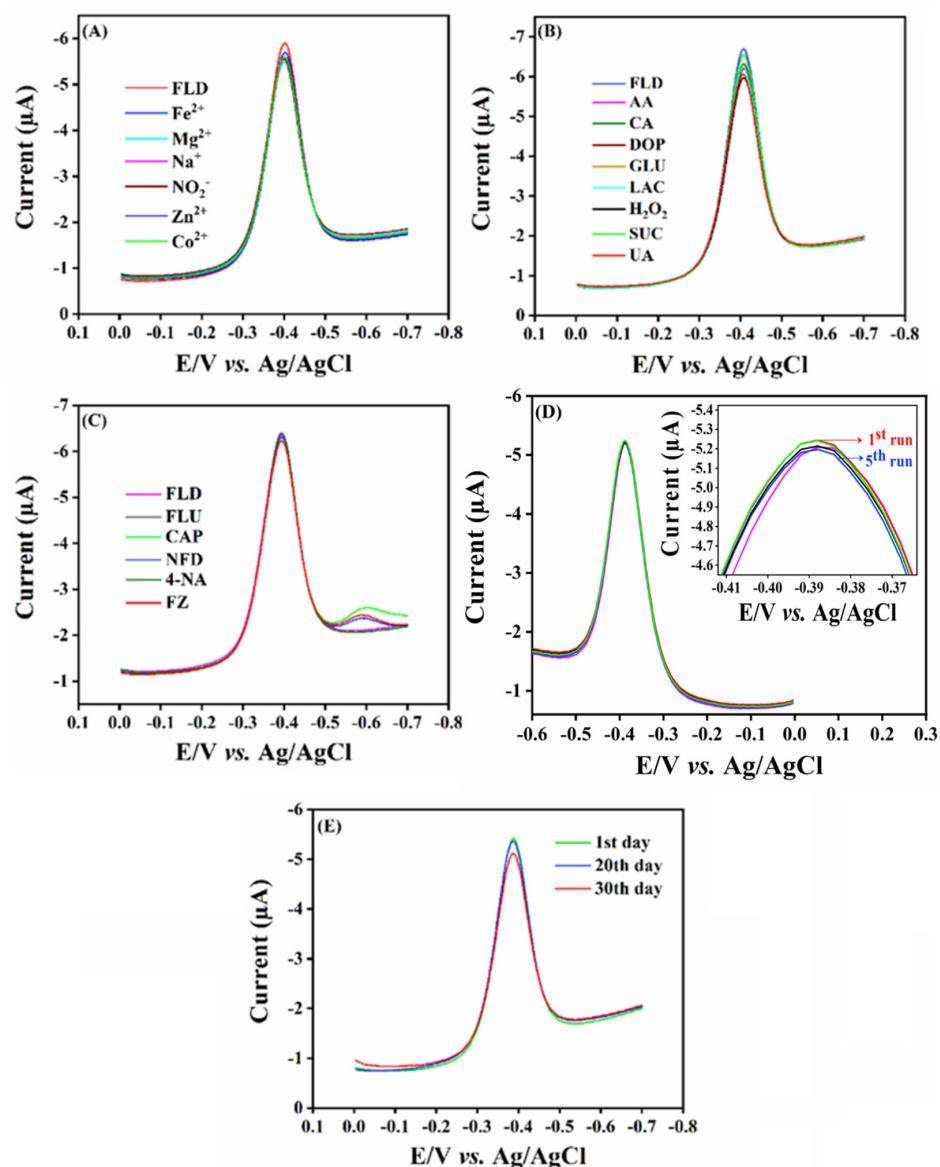


Figure 7. Cathodic current response for SrMnO₃/f-BN/SPCE with different interfering species, such as (A) metals ions, (B) biological molecules, and (C) nitro group related compounds. (D,E) Reproducibility and storage stability of SrMnO₃/f-BN/SPCE.

2.2.6. Real Sample Analysis

The practical usability of the designed sensor was examined using the DPV technique for the real-time detection of FLD in lake water and human urine samples. The lake water samples were collected from nearby Taipei Lake, and a human urine sample was collected from a healthy person. The collected real samples were free from FLD. Following the initial testing process, a known concentration of FLD was spiked into the samples. The prepared samples were used as a stock solution for further experimental analysis. The DPV

amplification waves were recorded for the consecutive addition of FLD concentrations from 20.0 to 100.0 μM from the prepared stock solutions. The obtained DPV results are displayed in Figure 8A,B; it can be seen that the developed sensor retains excellent electrocatalytic activity for the detection of FLD in real sample analysis, with good recovery results of about to 98.1–99.9%. The real sample analysis findings reveal that $\text{SrMnO}_3/\text{f-BN}/\text{SPCE}$ possesses ideal sensing properties for the detection of FLD. The recovery results are calculated using the standard addition method with three replicative measurements, and the obtained results are outlined in Table 2.

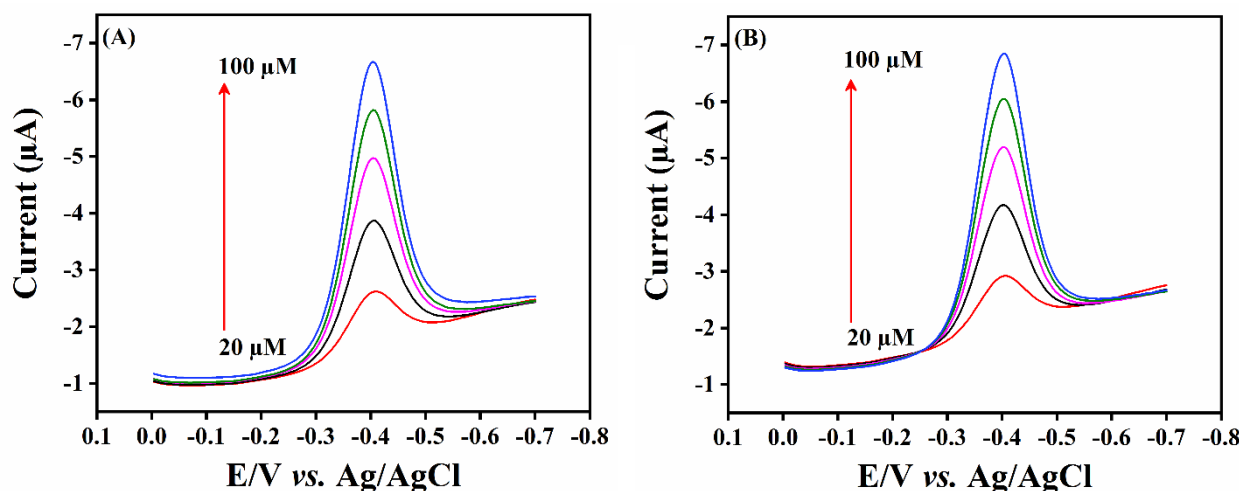


Figure 8. Real sample analysis in (A) human urine samples and (B) wastewater samples using $\text{SrMnO}_3/\text{f-BN}$ composite modified SPCE electrode.

Table 2. Practicality of FLD detection in spiked human urine and wastewater samples ($n = 3$).

Sample	Added (μM)	Found (μM)	Recoveries (%)
FLD spiked urine	20.0	19.8	99.0
	40.0	39.8	99.5
	60.0	58.9	98.2
	80.0	78.5	98.1
	100.0	98.7	98.7
FLD spiked wastewater	20.0	19.7	98.5
	40.0	39.9	99.8
	60.0	59.8	99.7
	80.0	79.9	99.9
	100.0	99.2	99.2

3. Experimental

3.1. Chemicals and Reagents

Analytical-grade strontium nitrate, manganese nitrate, potassium carbonate, FLD, NaH_2PO_4 , Na_2HPO_4 , h-BN, hydrogen peroxide (H_2O_2), and ethanol were purchased from Sigma-Aldrich Chemicals (Taipei, Taiwan) and used without further purification. Commercial screen-printed carbon electrodes (SPCE, model SE 100, working area: $5 \text{ mm}/0.196 \text{ cm}^2$) were purchased from Zensor R&D Co., Ltd. (Taichung City, Taiwan). The pH part of the electrochemical experiment was performed in 0.1 M phosphate buffer solution (PBS, pH 7).

3.2. Synthesis of SrMnO_3 Perovskite Microspheres

SrMnO_3 perovskite microspheres were synthesized by the co-precipitation method. In brief, about 50 mL each of strontium nitrate (0.05 M; 1.058 g) and manganese nitrate (0.05 M; 1.255 g) aqueous solution were sequentially added to a beaker with 100 mL of potassium bicarbonate (0.1 M; 2.7642 g) solution and then subjected to magnetic stirring

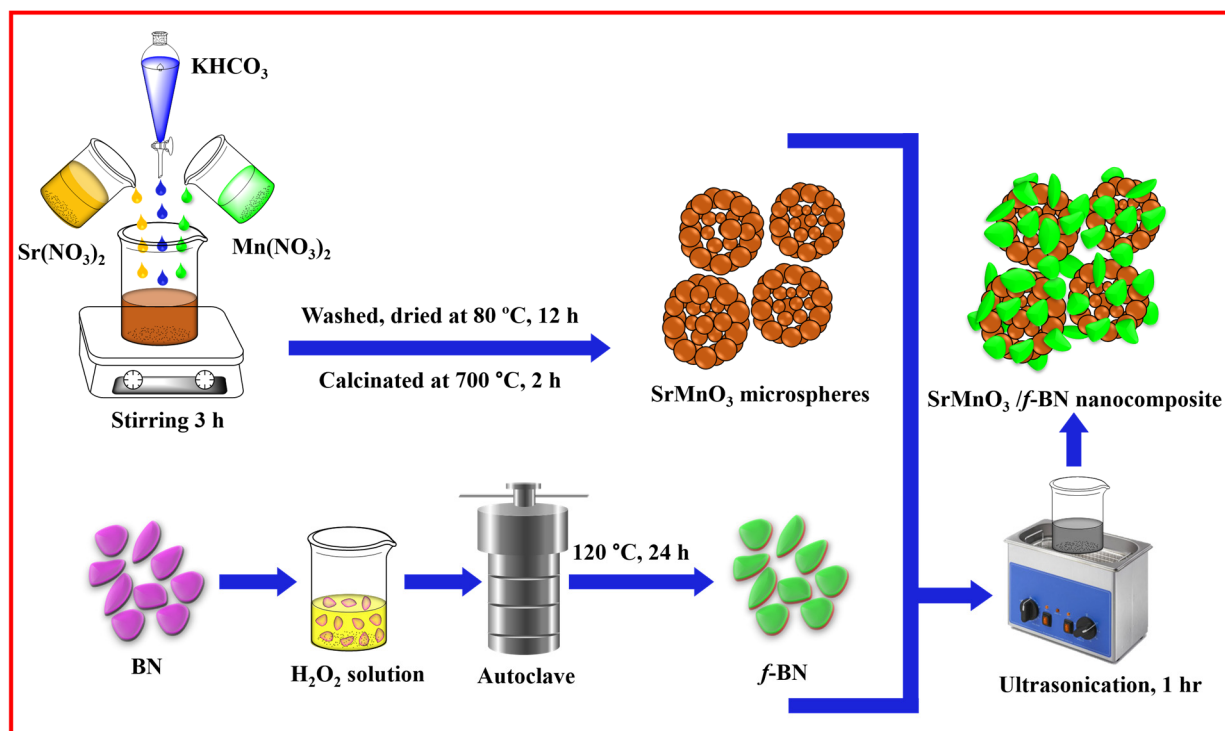
at ambient conditions for 3 h. During this time, the color of the mixed solution turned to a brown residue. The precipitate was collected by filtration and washed with deionized water (DI) and ethanol several times. The collected precipitate was dried in a hot oven at 80 °C for 12 h. Later, it was calcined at 700 °C (5 °C/min) for 2 h in an air atmosphere. The final obtained powder was denoted as SrMnO₃.

3.3. Functionalization of BN

Briefly, the as-received h-BN powder (1 mg/mL) was added to 200 mL H₂O₂ solution and then sonicated for 30 min to obtain a homogeneous dispersion. Then, the suspension was stirred at room temperature using a magnetic stirrer for 12 h. Then, the mixture was transferred to an autoclave container for thermal reaction at 120 °C, for 24 h. The final product was centrifuged and washed several times with DI water and then dried at 80 °C in an air oven for 6 h. The resultant powder was referred to as *f*-BN.

3.4. Synthesis of SrMnO₃/*f*-BN Composite

About 50 mg of as-prepared SrMnO₃ microsphere particles were dispersed in 50 mL DI water along with 10 mg of *f*-BN and ultra-sonicated for 1 h. The composite suspension was centrifuged and washed with DI water and ethanol several times. Afterwards, the resultant residue was dried at 60 °C for 24 h. The final product was called SrMnO₃/*f*-BN composite. The synthesis details are clearly described in Scheme 2.



Scheme 2. The schematic representation for the synthesis of SrMnO₃/*f*-BN composite.

3.5. Instrumentation

The X-ray diffraction (XRD) pattern study was analyzed using a Bruker D2 PHASER diffractometer (Karlsruhe, Germany) with Cu-K α radiation ($K = 1.54 \text{ \AA}$). Fourier transform-infra red (FT-IR) spectral data were recorded using FTIR-6600 spectroscopy (Easton, MD, USA). Raman spectra were examined using a confocal micro-Renishaw, 632 nm He-Ne laser source spectrometer (Gloucestershire, UK). The surface morphologies of the as-synthesized materials were analyzed using a field emission scanning electron microscope (FE-SEM: JEOL JSM-7610F Plus, Tokyo, Japan) equipped with energy-dispersive X-ray spectroscopy (EDAX). Brunauer-Emmett-Teller (BET) analysis for specific surface area measurement was

conducted using Micromeritics, Gemini VII (Monchegladbach, Germany) A conventional three-electrode system was employed using a CHI1205C and CHI900 potentiostat (CH Instruments, Inc., Austin, TX, USA), where Ag/AgCl (sat. KCl) was used as a reference electrode, modified screen-printed carbon electrode (SPCE) as a working electrode, and Pt-wire as a counter electrode.

3.6. Fabrication of the Sensor Electrode

The as-prepared SrMnO₃/f-BN composite powder (5 mg/mL) was added to a DI water-containing vial. A homogenous suspension was obtained after ultrasonication treatment for 30 min. Meanwhile, the surface of SPCE was gently washed with DI water and ethanol to remove the surface adsorbed dust particles, then dried naturally. About 6 µL of the catalyst suspension was drop-coated on the cleaned SPCE surface, followed by drying in an air oven at 80 °C for 10 min. The fabricated electrode was named SrMnO₃/f-BN/SPCE. Electrodes such as SrMnO₃/SPCE, BN/SPCE, and f-BN/SPCE were fabricated similarly for the control experiment. The fabricated electrodes were immersed in a deoxygenated electrolyte (0.1 M PBS, pH 7) system for sensing measurements.

4. Conclusions

In summary, we synthesized a facile and inexpensive composite based on SrMnO₃/f-BN for FLD detection. The above results obtained from electrochemical detection indicate that the developed sensor has superior catalytic activity and excellent analytical performance, with a wide linear range of 0.01–152.11 µM and a very low detection limit of 2.0 nM. Interestingly, the SrMnO₃/f-BN composite could be a promising candidate for the detection of FLD in both biological and pharmaceutical applications.

Supplementary Materials: The following supporting information can be downloaded at: <https://www.mdpi.com/article/10.3390/catal12121494/s1>, Figure S1: (A) BET surface area, nitrogen adsorption-desorption isotherm and (B) pore size distribution of SrMnO₃ (SMO, Red line), f-BN (blue line) and SMO/f-BN nanocomposite (black line). Figure S2: (A) FE-SEM mapping of SrMnO₃/f-BN nanocomposite, (B) Strontium (Sr), (C) Manganese (Mn), (D) Oxygen (O), (E) Boron (B), (F) Nitrogen (N). (G) represents of EDX spectrum of SrMnO₃/f-BN nanocomposite. Figure S3 (A&B) FE-SEM elemental mapping and EDX of BN, f-BN. Figure S4: The linear relation between cathodic peak potential (E_p) and various pH. Figure S5: (A) The linear relation between log scan rate (log v (mV/s) and log current (log I (µA)). (B) The linear relation between E_p and ln v.

Author Contributions: Conceptualization, K.V. and C.K.; methodology, S.S.; Software, K.V. and R.R.; validation, S.K.R.; formal analysis, K.V. and R.R.; investigation, R.R. and C.K.; Resources, S.-M.C. and C.-C.Y.; data curation, S.-M.C. and S.S.; writing – original draft, K.V. and R.R.; writing—review & editing, K.V., P.K., A.B., W.A.A.-O., N.P.K., C.K. and S.K.R.; visualization, A.B.; supervision, S.K.R.; project administration, C.-C.Y. and S.K.R.; funding acquisition, S.-M.C. and W.A.A.-O. All authors have read and agreed to the published version of the manuscript.

Funding: The authors acknowledge the Ministry of Science and Technology (MOST 110-2113-M-027-003), Taiwan, and extend their appreciation to the Researchers Supporting Project number (RSP2022R469), King Saud University, Riyadh, Saudi Arabia.

Data Availability Statement: Not available.

Acknowledgments: Krishnan Venkatesh acknowledges the Ministry of Education for the TEEP@AsiaPlus internship program and is grateful to Chun-Chen Yang, Battery Research Center of Green Energy, Ming Chi University of Technology, New Taipei City, Taiwan, for his supervision and instrument facilities.

Conflicts of Interest: The authors declare no conflict of interest.

References

1. Naghian, E.; Marzi Khosrowshahi, E.; Sohouli, E.; Ahmadi, F.; Rahimi-Nasrabadi, M.; Safarifard, V. A new electrochemical sensor for the detection of fentanyl lethal drug by a screen-printed carbon electrode modified with the open-ended channels of Zn(ii)-MOF. *New J. Chem.* **2020**, *44*, 9271–9277. [[CrossRef](#)]
2. Cooper, K.M.; Mulder, P.P.J.; van Rhijn, J.A.; Kovacsics, L.; McCracken, R.J.; Young, P.B.; Kennedy, D.G. Depletion of four nitrofurans antibiotics and their tissue-bound metabolites in porcine tissues and determination using LC-MS/MS and HPLC-UV. *Food Addit. Contam.* **2005**, *22*, 406–414. [[CrossRef](#)]
3. Wu, W.; Yang, S.; Liu, J.; Mi, J.; Dou, L.; Pan, Y.; Mujtaba Mari, G.; Wang, Z. Progress in immunoassays for nitrofurans detection. *Food Agric. Immunol.* **2020**, *31*, 890–909. [[CrossRef](#)]
4. Mahedero, M.C.; Díaz, T.G.; Pascual, S.G. Resolution of ternary mixtures of nitrofurantoin, furaltadone and furazolidone by partial least-square analysis to the spectrophotometric signals after photo-decomposition. *J. Pharm. Biomed. Anal.* **2002**, *29*, 477–485. [[CrossRef](#)] [[PubMed](#)]
5. Verdon, E.; Couedor, P.; Sanders, P. Multi-residue monitoring for the simultaneous determination of five nitrofurans (furazolidone, furaltadone, nitrofurazone, nitrofurantoin, nifursol) in poultry muscle tissue through the detection of their five major metabolites (AOZ, AMOZ, SEM, AHD, DNSA). *Anal. Chim. Acta* **2007**, *586*, 336–347. [[CrossRef](#)] [[PubMed](#)]
6. Hwa, K.Y.; Sharma, T.S.K. Nano assembly of NiFe spheres anchored on f-MWCNT for electrocatalytic reduction and sensing of nitrofurantoin in biological samples. *Sci. Rep.* **2020**, *10*, 12256. [[CrossRef](#)]
7. Díaz, T.G.; Cabanillas, A.G.; Valenzuela, M.I.A.; Correa, C.A.; Salinas, F. Determination of nitrofurantoin, furazolidone and furaltadone in milk by high-performance liquid chromatography with electrochemical detection. *J. Chromatogr. A* **1997**, *764*, 243–248. [[CrossRef](#)] [[PubMed](#)]
8. Barbosa, J.; Moura, S.; Barbosa, R.; Ramos, F.; da Silveira, M.I.N. Determination of nitrofurans in animal feeds by liquid chromatography-UV photodiode array detection and liquid chromatography-ionspray tandem mass spectrometry. *Anal. Chim. Acta* **2007**, *586*, 359–365. [[CrossRef](#)]
9. Chiu, S.H.; Su, Y.L.; Le, A.V.T.; Cheng, S.H. Nanocarbon material-supported conducting poly(melamine) nanoparticle-modified screen-printed carbon electrodes for highly sensitive determination of nitrofurans drugs by adsorptive stripping voltammetry. *Anal. Bioanal. Chem.* **2018**, *410*, 6573–6583. [[CrossRef](#)]
10. Khodari, M.; Salah El-Din, H.; Mersal, G.A.M. Electroreduction and quantification of furazolidone and furaltadone in different media. *Mikrochim. Acta* **2000**, *135*, 9–17. [[CrossRef](#)]
11. Wang, Q.; Chen, Z.; Chen, Y.; Cheng, N.; Hui, Q. Hydrogen storage in perovskite-type oxides ABO₃ for Ni/MH battery applications: A density functional investigation. *Ind. Eng. Chem. Res.* **2012**, *51*, 11821–11827. [[CrossRef](#)]
12. Sugahara, K.; Kamata, K.; Muratsugu, S.; Hara, M. Amino Acid-Aided Synthesis of a Hexagonal SrMnO₃ Nanoperovskite Catalyst for Aerobic Oxidation. *ACS Omega* **2017**, *2*, 1608–1616. [[CrossRef](#)] [[PubMed](#)]
13. Shen, Z.; Wang, X.; Luo, B.; Li, L. BaTiO₃-BiYbO₃ perovskite materials for energy storage applications. *J. Mater. Chem. A* **2015**, *3*, 18146–18153. [[CrossRef](#)]
14. Björketun, M.E.; Castelli, I.E.; Rossmesl, J.; Olsen, T.; Ukai, K.; Kato, M.; Dennler, G.; Jacobsen, K.W. Defect Chemistry and Electrical Conductivity of Sm-Doped La_{1-x}Sr_xCoO_{3-δ} for Solid Oxide Fuel Cells. *J. Phys. Chem. C* **2017**, *121*, 15017–15027. [[CrossRef](#)]
15. Liu, X.; Gong, H.; Wang, T.; Guo, H.; Song, L.; Xia, W.; Gao, B.; Jiang, Z.; Feng, L.; He, J. Cobalt-Doped Perovskite-Type Oxide LaMnO₃ as Bifunctional Oxygen Catalysts for Hybrid Lithium–Oxygen Batteries. *Chem. Asian J.* **2018**, *13*, 528–535. [[CrossRef](#)]
16. Atta, N.F.; El-Ads, E.H.; Galal, A.; Galal, A.E. Electrochemical Sensing Platform Based on Nano-Perovskite/Glycine/Carbon Composite for Amlodipine and Ascorbic Acid Drugs. *Electroanalysis* **2019**, *31*, 448–460. [[CrossRef](#)]
17. Vidya Rajan, N.; Alexander, L.K. Electrochemical sensing of modified ABO₃ perovskite: LaFe_{0.8}R_{0.2}O₃ (R= Cr, Co, Al). *AIP Conf. Proc.* **2017**, *1849*, 020027. [[CrossRef](#)]
18. Muthukutty, B.; Krishnapandi, A.; Chen, S.M.; Abinaya, M.; Elangovan, A. Innovation of Novel Stone-Like Perovskite Structured Calcium Stannate (CaSnO₃): Synthesis, Characterization, and Application Headed for Sensing Photographic Developing Agent Metol. *ACS Sustain. Chem. Eng.* **2020**, *8*, 4419–4430. [[CrossRef](#)]
19. Peña, M.A.; Fierro, J.L.G. Chemical structures and performance of perovskite oxides. *Chem. Rev.* **2001**, *101*, 1981–2017. [[CrossRef](#)]
20. El-Ads, E.H.; Galal, A.; Atta, N.F. The effect of A-site doping in a strontium palladium perovskite and its applications for non-enzymatic glucose sensing. *RSC Adv.* **2016**, *6*, 16183–16196. [[CrossRef](#)]
21. George, J.; Halali, V.V.; Sanjayan, C.G.; Suvina, V.; Sakar, M.; Balakrishna, R.G. Perovskite nanomaterials as optical and electrochemical sensors. *Inorg. Chem. Front.* **2020**, *7*, 2702–2725. [[CrossRef](#)]
22. Sunarso, J.; Hashim, S.S.; Zhu, N.; Zhou, W. Perovskite oxides applications in high temperature oxygen separation, solid oxide fuel cell and membrane reactor: A review. *Prog. Energy Combust. Sci.* **2017**, *61*, 57–77. [[CrossRef](#)]
23. Das, N.; Kandimalla, S. Application of perovskites towards remediation of environmental pollutants: An overview: A review on remediation of environmental pollutants using perovskites. *Int. J. Environ. Sci. Technol.* **2017**, *14*, 1559–1572. [[CrossRef](#)]
24. Gholamrezaei, S.; Amiri, M.; Amiri, O.; Salavati-Niasari, M.; Moayedi, H. Ultrasound-accelerated synthesis of uniform SrMnO₃ nanoparticles as water-oxidizing catalysts for water splitting systems. *Ultrason. Sonochem.* **2020**, *62*, 104899. [[CrossRef](#)] [[PubMed](#)]
25. Shanmugavadivel, M.; Dhayabaran, V.V.; Subramanian, M. Nanosized BaMnO₃ as high performance supercapacitor electrode material: Fabrication and characterization. *Mater. Lett.* **2016**, *181*, 335–339. [[CrossRef](#)]

26. Huang, X.; Zhang, Q.; Chang, H.; Gan, J.; Yue, H.; Yang, Y. Hydrothermal Synthesis of Nanosized $\text{LiMnO}_2\text{-Li}_2\text{MnO}_3$ Compounds and Their Electrochemical Performances. *J. Electrochem. Soc.* **2009**, *156*, A162. [[CrossRef](#)]
27. Jin, Z.; Bard, A.J. Surface Interrogation of Electrodeposited MnO_x and CaMnO_3 Perovskites by Scanning Electrochemical Microscopy: Probing Active Sites and Kinetics for the Oxygen Evolution Reaction. *Angew. Chem. Int. Ed.* **2021**, *60*, 794–799. [[CrossRef](#)] [[PubMed](#)]
28. Tan, P.; Liu, M.; Shao, Z.; Ni, M. Recent Advances in Perovskite Oxides as Electrode Materials for Nonaqueous Lithium–Oxygen Batteries. *Adv. Energy Mater.* **2017**, *7*, 1602674. [[CrossRef](#)]
29. Zhu, H.; Xu, X.; Zhong, X. Fabrication and Characterization of Hexagonal SrMnO_3 Nanofibers by Electrospinning. *MATEC Web Conf.* **2016**, *67*, 06093. [[CrossRef](#)]
30. Wang, H.; Gao, S.M.; Xu, J.W.; Yuan, C.L.; Zhang, X.W. Synthesis and resistive switching behaviour of ZnMnO_3 thin films with an $\text{Ag/ZnMnO}_3/\text{ITO}$ unsymmetrical structure. *Bull. Mater. Sci.* **2015**, *38*, 105–109. [[CrossRef](#)]
31. Shafi, P.M.; Joseph, N.; Karthik, R.; Shim, J.; Bose, A.C.; Ganesh, V. Lemon juice-assisted synthesis of LaMnO_3 perovskite nanoparticles for electrochemical detection of dopamine. *Microchem. J.* **2021**, *164*, 105945. [[CrossRef](#)]
32. Li, Y.J.; Yang, C. Solid-State Ball-Milling of Co_3O_4 Nano/Microspheres and Carbon Black Endorsed LaMnO_3 Perovskite Catalyst for Bifunctional Oxygen Electrocatalysis. *Catalysts* **2021**, *11*, 762021.
33. Celorrio, V.; Calvillo, L.; Granozzi, G.; Russell, A.E.; Fermin, D.J. AMnO_3 (A = Sr, La, Ca, Y) Perovskite Oxides as Oxygen Reduction Electrocatalysts. *Top. Catal.* **2018**, *61*, 154–161. [[CrossRef](#)] [[PubMed](#)]
34. Zhang, M.; Jeerh, G.; Zou, P.; Lan, R.; Wang, M.; Wang, H.; Tao, S. Recent development of perovskite oxide-based electrocatalysts and their applications in low to intermediate temperature electrochemical devices. *Mater. Today* **2021**, *49*, 351–377. [[CrossRef](#)]
35. George, G.; Jackson, S.L.; Luo, C.Q.; Fang, D.; Luo, D.; Hu, D.; Wen, J.; Luo, Z. Effect of doping on the performance of high-crystalline SrMnO_3 perovskite nanofibers as a supercapacitor electrode. *Ceram. Int.* **2018**, *44*, 21982–21992. [[CrossRef](#)]
36. Doroftei, C.; Leontie, L. Nanocrystalline SrMnO_3 perovskite prepared by sol–gel self-combustion method for sensor applications. *J. Sol-Gel Sci. Technol.* **2021**, *97*, 146–154. [[CrossRef](#)]
37. Kostopoulou, A.; Brintakis, K.; Nasikas, N.K.; Stratakis, E. Perovskite nanocrystals for energy conversion and storage. *Nanophotonics* **2019**, *8*, 1607–1640. [[CrossRef](#)]
38. Hong, J.; Aphale, A.N.; Heo, S.J.; Hu, B.; Reiser, M.; Belko, S.; Singh, P. Strontium Manganese Oxide Getter for Capturing Airborne Cr and S Contaminants in High-Temperature Electrochemical Systems. *ACS Appl. Mater. Interfaces* **2019**, *11*, 34878–34888. [[CrossRef](#)]
39. Assirey, E.A.R. Perovskite synthesis, properties and their related biochemical and industrial application. *Saudi Pharm. J.* **2019**, *27*, 817–829. [[CrossRef](#)]
40. Nielsen, M.B.; Ceresoli, D.; Parisiades, P.; Prakapenka, V.B.; Yu, T.; Wang, Y.; Bremholm, M. Phase stability of the SrMnO_3 hexagonal perovskite system at high pressure and temperature. *Phys. Rev. B Condens. Matter Mater. Phys.* **2014**, *90*, 214101. [[CrossRef](#)]
41. Sacchetti, A.; Baldini, M.; Postorino, P.; Martin, C.; Maignan, A. Raman spectroscopy on cubic and hexagonal SrMnO_3 . *J. Raman Spectrosc.* **2006**, *37*, 591–596. [[CrossRef](#)]
42. Sacchetti, A.; Baldini, M.; Crispoldi, F.; Postorino, P.; Dore, P.; Martin, N.C.; Maignan, A. Temperature dependence of the optical phonons in SrMnO_3 manganite: Evidence of a low-temperature structural transition in the hexagonal compound. *Phys. Rev. B Condens. Matter Mater. Phys.* **2005**, *72*, 172407. [[CrossRef](#)]
43. dos Santos, O.A.L.; Sneha, M.; Devarani, T.; Bououdina, M.; Backx, B.P.; Vijaya, J.J.; Bellucci, S. Review—Perovskite/Spinel Based Graphene Derivatives Electrochemical and Biosensors. *J. Electrochem. Soc.* **2021**, *168*, 067506. [[CrossRef](#)]
44. Chen, T.-W.; Ramachandran, R.; Chen, S.-M.; Anushya, G.; Divya Rani, S.; Mariyappan, V.; Elumalai, P.; Vasimalai, N. High-performance-based perovskite-supported nanocomposite for the development of green energy device applications: An overview. *Nanomaterials* **2021**, *11*, 1006. [[CrossRef](#)]
45. Ahmad, K.; Mohammad, A.; Mathur, P.; Mobin, S.M. Preparation of SrTiO_3 perovskite decorated rGO and electrochemical detection of nitroaromatics. *Electrochim. Acta* **2016**, *215*, 435–446. [[CrossRef](#)]
46. Zhang, J.; Feng, J.; Tian, Y.; Wu, Y.; Liu, X.; He, Q. Ultrasensitive electrochemical determination of tyrosine based on the $\alpha\text{-Fe}_2\text{O}_3@ \text{Co}_3\text{O}_4\text{-NRGO}$ modified electrode. *Microchem. J.* **2021**, *171*, 106867. [[CrossRef](#)]
47. Liu, J.; Sun, L.; Li, G.; Hu, J.; He, Q. Ultrasensitive detection of dopamine via electrochemical route on spindle-like $\alpha\text{-Fe}_2\text{O}_3$ Mesocrystals/rGO modified GCE. *Mater. Res. Bull.* **2021**, *133*, 111050. [[CrossRef](#)]
48. Govindasamy, M.; Wang, S.F.; Pan, W.C.; Subramanian, B.; Ramalingam, R.J.; Al-lohedan, H. Facile sonochemical synthesis of perovskite-type SrTiO_3 nanocubes with reduced graphene oxide nanocatalyst for an enhanced electrochemical detection of α -amino acid (tryptophan). *Ultrason. Sonochem.* **2019**, *56*, 193–199. [[CrossRef](#)]
49. Bi, Y.S.; Liu, B.; Liu, X.Y.; Qin, Y.; Zou, B.X. A h-BCN for electrochemical sensor of dopamine and uric acid. *J. Nanomater.* **2020**, *2020*, 4604820. [[CrossRef](#)]
50. Maity, C.K.; Sahoo, S.; Verma, K.; Behera, A.K.; Nayak, G.C. Facile functionalization of boron nitride (BN) for the development of high-performance asymmetric supercapacitors. *New J. Chem.* **2020**, *44*, 8106–8119. [[CrossRef](#)]
51. Bhimanapati, G.R.; Kozuch, D.; Robinson, J.A. Large-scale synthesis and functionalization of hexagonal boron nitride nanosheets. *Nanoscale* **2014**, *6*, 11671–11675. [[CrossRef](#)] [[PubMed](#)]

52. Chen, L.; Xu, H.F.; He, S.J.; Du, Y.H.; Yu, N.J.; Du, X.Z.; Lin, J.; Nazarenko, S. Thermal conductivity performance of polypropylene composites filled with polydopamine-functionalized hexagonal boron nitride. *PLoS ONE* **2017**, *12*, 0170523. [[CrossRef](#)] [[PubMed](#)]
53. Tang, C.; Bando, Y.; Huang, Y.; Zhi, C.; Golberg, D. Synthetic routes and formation mechanisms of spherical boron nitride nanoparticles. *Adv. Funct. Mater.* **2008**, *18*, 3653–3661. [[CrossRef](#)]
54. Su, Z.; Wang, H.; Ye, X.; Tian, K.; Huang, W.; He, J.; Guo, Y.; Tian, X. Synergistic enhancement of anisotropic thermal transport flexible polymer composites filled with multi-layer graphene (mG) and mussel-inspired modified hexagonal boron nitride (h-BN). *Compos. Part A Appl. Sci. Manuf.* **2018**, *111*, 12–22. [[CrossRef](#)]
55. Li, Q.; Huo, C.; Yi, K.; Zhou, L.; Su, L.; Hou, X. Preparation of flake hexagonal BN and its application in electrochemical detection of ascorbic acid, dopamine and uric acid. *Sens. Actuators B Chem.* **2018**, *260*, 346–356. [[CrossRef](#)]
56. Jesu Amalraj, A.J.; Narasimha Murthy, U.; Sea-Fue, W. Ultrasensitive electrochemical detection of an antibiotic drug furaltadone in fish tissue with a ZnO-ZnCo₂O₄ self-assembled nano-heterostructure as an electrode material. *Microchem. J.* **2021**, *169*, 106566. [[CrossRef](#)]
57. Vasu, D.; Karthi Keyan, A.; Sakthinathan, S.; Chiu, T.W. Investigation of electrocatalytic and photocatalytic ability of Cu/Ni/TiO₂/MWCNTs Nanocomposites for detection and degradation of antibiotic drug Furaltadone. *Sci. Rep.* **2022**, *12*, 886. [[CrossRef](#)]
58. Balamurugan, K.; Rajakumaran, R.; Chen, S.M.; Karthik, R.; Shim, J.J.; Shafi, P.M. Massive engineering of spinel cobalt tin oxide/tin oxide-based electrocatalyst for the selective voltammetric determination of antibiotic drug furaltadone in water samples. *J. Alloys Compd.* **2021**, *882*, 160750. [[CrossRef](#)]
59. Rajakumaran, R.; Musuvadhi Babulal, S.; Ming Chen, S.; Sukanya, R.; Karthik, R.; Muhammed Shafi, P.; Shim, J.-J.; Yo-Shiuana, C. Ingenious design of iron vanadate engulfed 3D porous reduced graphene oxide nanocomposites as a reliable electrocatalyst for the selective amperometric determination of furaltadone in aquatic environments. *Appl. Surf. Sci.* **2021**, *569*, 151046. [[CrossRef](#)]